


# Implications of Warm Rain in Shallow Cumulus and Congestus Clouds for Large-Scale Circulations

Louise Nuijens<sup>1</sup>  · Kerry Emanuel<sup>2</sup> · Hirohiko Masunaga<sup>3</sup> · Tristan L'Ecuyer<sup>4</sup>

Received: 15 February 2017 / Accepted: 18 September 2017 / Published online: 27 September 2017  
© The Author(s) 2017. This article is an open access publication

**Abstract** Space-borne observations reveal that 20–40% of marine convective clouds below the freezing level produce rain. In this paper we speculate what the prevalence of warm rain might imply for convection and large-scale circulations over tropical oceans. We present results using a two-column radiative–convective model of hydrostatic, non-linear flow on a non-rotating sphere, with parameterized convection and radiation, and review ongoing efforts in high-resolution modeling and observations of warm rain. The model experiments investigate the response of convection and circulation to sea surface temperature (SST) gradients between the columns and to changes in a parameter that controls the conversion of cloud condensate to rain. Convection over the cold ocean collapses to a shallow mode with tops near 850 hPa, but a congestus mode with tops near 600 hPa can develop at small SST differences when warm rain formation is more efficient. Here, interactive radiation and the response of the circulation are crucial: along with congestus a deeper moist layer develops, which leads to less low-level radiative cooling, a smaller buoyancy gradient between the columns, and therefore a weaker circulation and less subsidence over the cold ocean. The congestus mode is accompanied with more surface precipitation in the subsiding column and less surface precipitation in the deep convecting column. For the shallow mode over colder oceans, circulations also weaken with more efficient warm rain formation, but only marginally. Here, more warm rain reduces convective tops and the boundary layer depth—similar to Large-Eddy Simulation (LES) studies—which reduces the integrated buoyancy gradient. Elucidating the impact of warm rain can benefit from large-domain high-resolution simulations and observations. Parameterizations of warm rain may be constrained through collocated cloud and rain profiling from ground, and concurrent changes in convection and rain in subsiding and

---

✉ Louise Nuijens  
louise.nuijens@tudelft.nl

<sup>1</sup> Delft University of Technology, 2628 CN Delft, Netherlands

<sup>2</sup> Massachusetts Institute of Technology, Cambridge, MA 02139, USA

<sup>3</sup> Nagoya University, Nagoya 464-8601, Japan

<sup>4</sup> University of Wisconsin-Madison, Madison, WI 53706, USA

convecting branches of circulations may be revealed from a collocation of space-borne sensors, including the Global Precipitation Measurement (GPM) and upcoming Aeolus missions.

**Keywords** Warm rain · Shallow cumulus · Congestus · Circulations · Climate

## 1 Introduction

Before observations demonstrated that clouds with tops below the freezing level are raining (Byers and Hall 1955; Battan and Braham 1956), scientists believed that ice nuclei are necessary to produce rain. Inspired by those observations, scientists soon discovered the importance of coalescence processes for warm rain formation. Coalescence processes also helped explain why clouds over oceans with a similar depth as clouds over land rain more easily. Namely, oceans are deprived of aerosol, except for sea salt and sulfate. Hence, there are relatively few cloud condensation nuclei over oceans, so that cloud droplets are relatively large, and auto-conversion and accretion processes are very efficient (Kubar et al. 2009).

In the subtropics and tropics, the freezing level is located between 4 and 5 km, and raining clouds include subtropical stratocumulus over cold eastern ocean boundaries; shallow cumulus clouds that are more widespread throughout the subtropics and tropics; and congestus clouds, which tend to be confined to warmer oceans. According to the WMO cloud atlas, congestus is not a cloud type on its own, but a species of cumulus with tops between 2 km and the freezing level (although in the literature congestus is often used to denote cumuli with tops up to 8 km). Although both shallow cumulus and congestus produce drizzle and rain alike, a point we return to below, the distinction is useful, because congestus appears more sensitive to changing large-scale states (Nuijens et al. 2014).

The CloudSat cloud profiling radar (CPR), which is currently the only sensor capable of delineating warm cloud, drizzle and rain, has demonstrated that oceans are covered by 10–50% of warm clouds (Fig. 1a). Of these warm clouds, between 20 and 40% contain

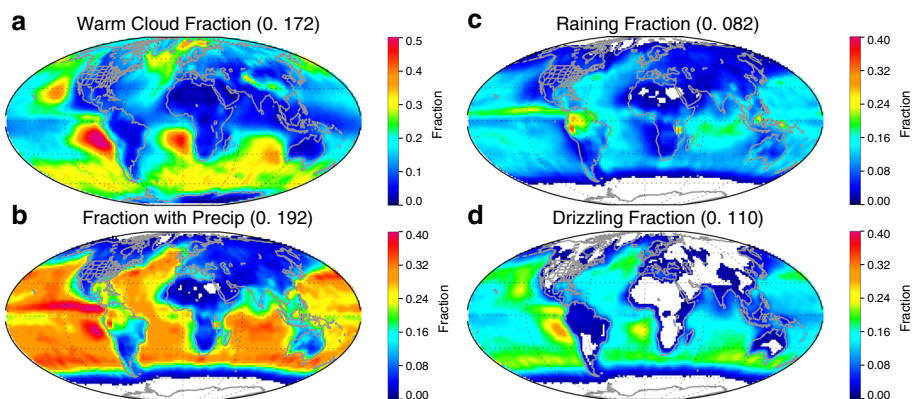


**Fig. 1** Global warm rain occurrence observed by CloudSat during 2007–2010. Warm clouds are as those with tops  $>273$  K. Drizzle is defined as having a “near-surface” (the lowest detectable range bin in CloudSat observations) reflectivity  $Z$  greater than  $-7.5$  dBZ, while rain is defined as  $Z > 0$  dBZ. The rain and drizzle fractions represent the fraction of warm clouds that contain rain or drizzle, respectively. CloudSat data are processed using the 2C-PRECIP-COLUMN and 2C-RAIN-PROFILE algorithms described in Haynes et al. (2009) and Lebsock and L’Ecuyer (2011), respectively

precipitation (Fig. 1b). Somewhat lower fractions are found near ocean boundaries and higher fractions in the Eastern Pacific, but overall most regions have clouds with a precipitating fraction of at least 5–10%. Figure 1c, d further separates precipitation in drizzle and rain, which shows that drizzle is widespread and concentrated over eastern ocean boundaries, whereas rain is concentrated in the downstream trades and near the Inter-tropical convergence zone (ITCZ), e.g., just north of the Equator in the Pacific and Atlantic oceans, or just south of the Equator in the Indian ocean.

One might not be impressed by those numbers. But those who live on islands have long appreciated the occasional passing of warm rain showers, which on windward sides of hilly islands make for lush vegetation, even during the “dry” season when deep convection abates.

Measurements from the precipitation radar (PR) deployed during the Tropical Rainfall Measuring Mission (TRMM, 1997–2015) first emphasized the prevalence of warm rain over global oceans and their potential impact on large-scale heating rates (Short and Nakamura 2000; Schumacher and Houze 2003; Takayabu et al. 2010). But the TRMM PR has a minimum detection threshold of about 0.4–0.5 mm h<sup>-1</sup> and therefore misses about 9% of accumulated rain and up to 50% of the occurrence of light rain compared to CloudSat (Berg et al. 2009). Global precipitation estimates from passive microwave sensors also lack a sensitivity to light rain, especially when rain covers only small areas, which is the case for isolated cumulus showers (Burdanowitz et al. 2015). The most widely used Global Precipitation Climatology Project (GPCP) product has long been used to derive surface latent heat fluxes to construct the global mean energy budget, and a lack of warm rain might explain why observed heat fluxes at the ocean surface have not matched observed ocean heating rates. By increasing global precipitation rates by about 16% based on CloudSat data, equivalent to increasing the latent heat flux by 12 W m<sup>-2</sup>, the global mean surface energy budget can be closed (Stephens et al. 2012). But warm rain is probably not the only reason for residuals in the surface energy budget. Largest residuals are found in regions where shallow cumuli dominate but alternate with deeper convection (Kato et al. 2016), but these residuals are larger than warm rain can account for. One hypothesis is that retrieval errors are caused by greater variability in deeper convection along with shallow convection, which warrants a better understanding of the coupling between different types of convection.

Warm rain may also alter the radiation budget by influencing the microphysical and mesoscale structure of clouds, which satellite images, corroborated by in-situ measurements and high-resolution modeling, have demonstrated. Numerous cells of seemingly cloud-free air (pockets of open cells, POCs) surrounded by walls of drizzle can be embedded into an otherwise homogeneous stratocumulus cloud deck (Stevens et al. 2005; Wood et al. 2008). In these cells cloud droplets have been scavenged by drizzle drops, leading to very low cloud droplet number concentrations. Observations have also demonstrated that fields of shallow cumuli accompanied by significant rain are organized into arc-shaped formations (Snodgrass et al. 2009; Zuidema et al. 2012). These are representative for the presence of cold pools, which are produced by the evaporation of rain and convective downdrafts, similar to the cold pools that accompany deep convection (Tompkins 2001).

When rain evaporates, it no longer produces a net (latent) heating, and it redistributes moisture in the atmosphere. The relative fraction of rain that evaporates or reaches the surface is thus important for large-scale heat and moisture budgets. Herbert Riehl derived the first heat budget of the trades and argued that each layer of the lower atmosphere would

precipitate (and heat) just as much as would be required to balance the loss of heat from radiation. Hence, from the profile of radiative cooling, one could predict the profile of the rain flux and thus the profile of the moisture flux (Riehl et al. 1951).

But, since Riehl's study, not much research has focused on large-scale controls and impacts of warm rain. More attention has been given to microphysical aspects of warm rain, including the role of aerosols in the onset of warm rain. For instance, aerosol and cloud condensation nuclei (CCN) concentrations control the height at which rain-sized drops first start to form. Figure 2, adopted from Lonitz et al. (2015), shows how radar reflectivity, which measures the sixth moment of the drop-size distribution, increases with height above cloud base for different CCN concentrations. The gray lines illustrate theoretical behavior, assuming a gamma distribution of the drop-size distribution, and the black lines illustrate the behavior of a 1D kinematic bin microphysics model (Seifert and Stevens 2010). According to the CloudSat definition, a reflectivity larger than  $-7$  dBZ corresponds to drizzle, which implies that for a CCN concentration of  $100\text{ cm}^{-3}$  drizzle forms when clouds reach 1.7 km. Indeed, the percentage of clouds that develop a maximum reflectivity larger than  $-7$  dBZ (drizzle) or 0 dBZ (rain) increases substantially for cloud tops beyond 1.5 km (Fig. 2b): 20% of clouds contain drizzle, and 20% contain rain. For cloud tops beyond 2 km, most clouds already contain rain (82%).

Warm rain is thus an integral part of shallow convection, which may influence climate in ways that are not yet well measured or modeled on a global scale. Do we understand how the presence of warm rain changes the character of warm clouds and the large-scale circulations in which these clouds are embedded? And what regulates variations in the depth of the convection?

To formulate ideas about the interaction between convection, warm rain and circulations, a conceptual model can be helpful and bypass some of the complexities of global

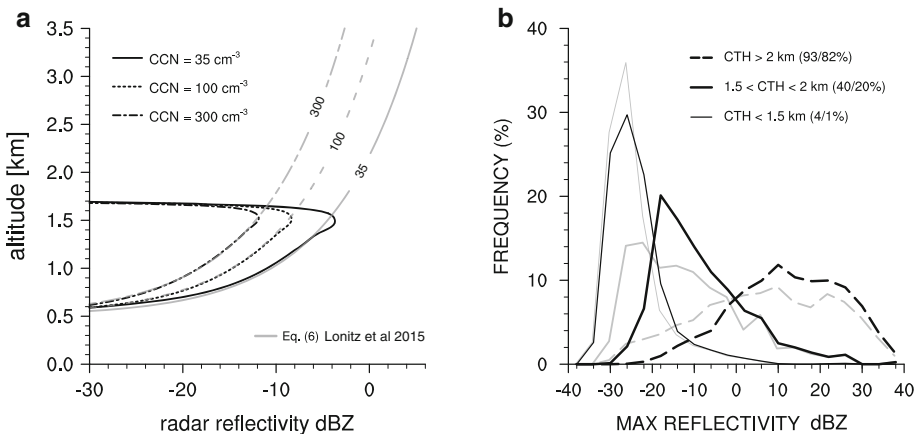


**Fig. 2** On the left: the increase in radar reflectivity, a measure of the sixth moment of the rain-drop-size distribution, with height in developing (not-raining) clouds as simulated with a kinematic 1D bin model of microphysics (black lines) and from theory assuming a gamma distribution for the rain-drop-size distribution (gray lines). The figure is adopted from an earlier version in Lonitz et al. (2015). On the right: distributions of the maximum radar reflectivity found anywhere in individual cloud entities with a cloud base  $< 800$  m, as observed at the Barbados Cloud Observatory during 3 years. The distributions in black are for three cloud top height (CTH) categories, and percentages indicate the total number of clouds (in %) which have a maximum reflectivity  $\geq -7$  dBZ/ $\geq 0$  dBZ. The distributions in light gray are for maximum reflectivities below cloud base only

models. In this paper we use a two-column radiative–convective equilibrium (RCE) model to do so, and Sect. 2 introduces the model and presents first results. Even with such a simplified framework, the interaction between circulation and convection appears intricate, but we will speculate on a few mechanisms that can be tested in further studies or evaluated in models with explicit convection or observations. In Sect. 3 we will discuss ongoing efforts in fine-scale modeling of convection (Large-Eddy Simulations), spaceborne and ground-based observations, and we summarize our thoughts in Sect. 4.

## 2 Warm Rain in Large-Scale Circulations

The prevalence of warm rain demands a better understanding of what warm rain implies for the structure of the lower atmosphere and the energy budget of subtropical and tropical oceans. Because regions with warm clouds are connected to regions with cold clouds through large-scale circulations, the influence of warm rain may also be felt remotely.

A number of studies have hinted that shallow convection can have far-reaching effects. For instance, in an idealized model of tropical climate shallow convection is responsible for the ventilation of boundary layer humidity, which affects the width and the intensity of the intertropical convergence zone (Neggers et al. 2007). Shallow convective mixing is also an attractive tuning factor in numerical weather prediction and global models, because it can substantially influence global distributions of liquid water, cloudiness and the radiation budget (Bechtold et al. 2014; Mauritsen et al. 2012). Even the climate sensitivity of a global model appears to be strongly regulated by local mixing by shallow convection and large-scale shallow overturning circulations (Sherwood et al. 2014). An important process underlying these far-reaching effects is the radiative cooling of the cloud-topped boundary layer. Stronger cloud-radiative effects in the subsiding branch of Walker circulations have been shown to narrow the area of deep convection in the upward branch (Bretherton and Sobel 2002; Peters and Bretherton 2005). Cloud-radiative effects also help aggregate deep convection in cloud-resolving and large eddy simulation (LES) models in radiative-convective equilibrium (RCE) (Muller and Held 2012; Wing and Emanuel 2014; Hohenegger and Stevens 2016).

Observations also show hints that differences in the characteristics of rain are accompanied by differences in the circulation. When shallow overturning circulations in the tropical Eastern Pacific are stronger, the Eastern Pacific is characterized by more large clusters of rain, whereas weaker shallow circulations are accompanied with a larger fraction of smaller isolated raining cells (Chen and Liu 2015). Such findings suggest that important feedbacks between regions of warm and cold cloud may exist, which include not only the vertical structure of moisture and cloud, but also rain.

Ideally global climate models (GCMs) would provide us insight into such feedbacks. But GCMs already disagree on the shallow convection that precedes warm rain (Sherwood et al. 2014) and their complexity makes it challenging to isolate processes. Instead, we aim for a more simplified setting following a series of studies that have used idealized two-box or four-box equilibrium models to study the sensitivity of tropical climate. Notably, Pierrehumbert (1995) demonstrated that the interaction between dry subsiding regions and moist convecting regions is an important determinant of tropical climate. His study and that of others (Miller 1997; Larson et al. 1999) also emphasize the strong sensitivity of tropical circulations to water vapor, cloudiness and radiative cooling in the subsiding region. Other factors that are important for circulation strength are the relative area

occupied by subsiding versus convecting areas (Pierrehumbert 1995; Bellon and Le Treut 2003), e.g., the relative size of the two boxes, and the sea surface temperature (SST) gradients as set by surface winds and ocean transport (Sun and Liu 1996; Clement and Seager 1999).

In our first exploration of the sensitivity of circulations to warm rain, we use an extension of a one-dimensional (single-column) RCE model, which numerically solves the hydrostatic equations of motion for non-rotating, nonlinear flow in two side-by-side columns. Rather than assuming convection in the subsiding column is limited to the boundary layer, as in most of the two-column model studies just mentioned, the depth of convection is calculated interactively by the convection scheme. Furthermore, radiation is interactive and a cloud scheme is used. A version of this model for linear flow was first used by Nilsson and Emanuel (1999), which demonstrated that a positive feedback between the circulation, clear-sky water vapor and radiation can destabilize radiative–convective equilibrium and attain a new equilibrium with a thermally direct circulation between the columns. In our simplified setup we prescribe SST gradients, and the two columns are of equal size. The latter is a shortcoming of the model setup that we are aware of. The model also uses parameterized physics and thus carries similar uncertainties as the physics used in GCMs. Nevertheless, the simplified geometry of the model allows us to get a first insight into mechanisms that may be relevant to warm rain in circulations, which we hope are further tested in future studies. The next section describes the model and its setup in more detail.

## 2.1 A Two-Column RCE Model

The model's columns are oriented in a  $x, z$  plane, and the following equations for temperature  $T$ , specific humidity  $q_v$  and the vorticity  $\eta$  are solved by time integration:

$$\frac{\partial T}{\partial t} + u \frac{\partial T}{\partial x} + \omega \frac{\partial T}{\partial p} + \frac{\alpha \omega}{c_p} = \gamma \frac{\partial^2 T}{\partial x^2} + F_{SH} + F_R + F_{Q1} \quad (1)$$

$$\frac{\partial q_v}{\partial t} + u \frac{\partial q_v}{\partial x} + \omega \frac{\partial q_v}{\partial p} = \gamma \frac{\partial^2 q_v}{\partial x^2} + F_{LH} + F_{Q2} \quad (2)$$

$$\frac{\partial \eta}{\partial t} + u \frac{\partial \eta}{\partial x} + f \frac{\partial v}{\partial p} = \frac{\partial \alpha}{\partial x} + \gamma \frac{\partial^2 \eta}{\partial x^2} + \frac{\partial v(\partial \eta / \partial p)}{\partial p} + \frac{\partial F_c^u}{\partial p} \quad (3)$$

whereby the vorticity  $\eta$  of the flow is defined as:

$$\eta = \frac{\partial u}{\partial p} - \frac{\partial \omega}{\partial x} \quad (4)$$

and the specific volume  $\alpha$  as:

$$\alpha = \frac{T R_d (1 - q_v + q_v / \epsilon)}{p} \quad (5)$$

Here,  $R_d$  is the gas constant for dry air and  $\epsilon$  is the ratio of the molecular mass of water vapor and of dry air. Furthermore,  $u$  is the zonal wind;  $\omega$  is the vertical velocity in pressure coordinates;  $c_p$  is the specific heat capacity of dry air;  $F_{SH}$  and  $F_{LH}$  are the sensible and latent heat fluxes at the surface;  $F_R$  is the net radiative heating tendency;  $F_{Q1}$  and  $F_{Q2}$  are the heat source and moisture source/sink due to convection and condensation;  $f$  is the Coriolis parameter;  $\gamma$  represents the inverse of a damping timescale  $\tau$ ;  $F_c^u$  is the tendency of

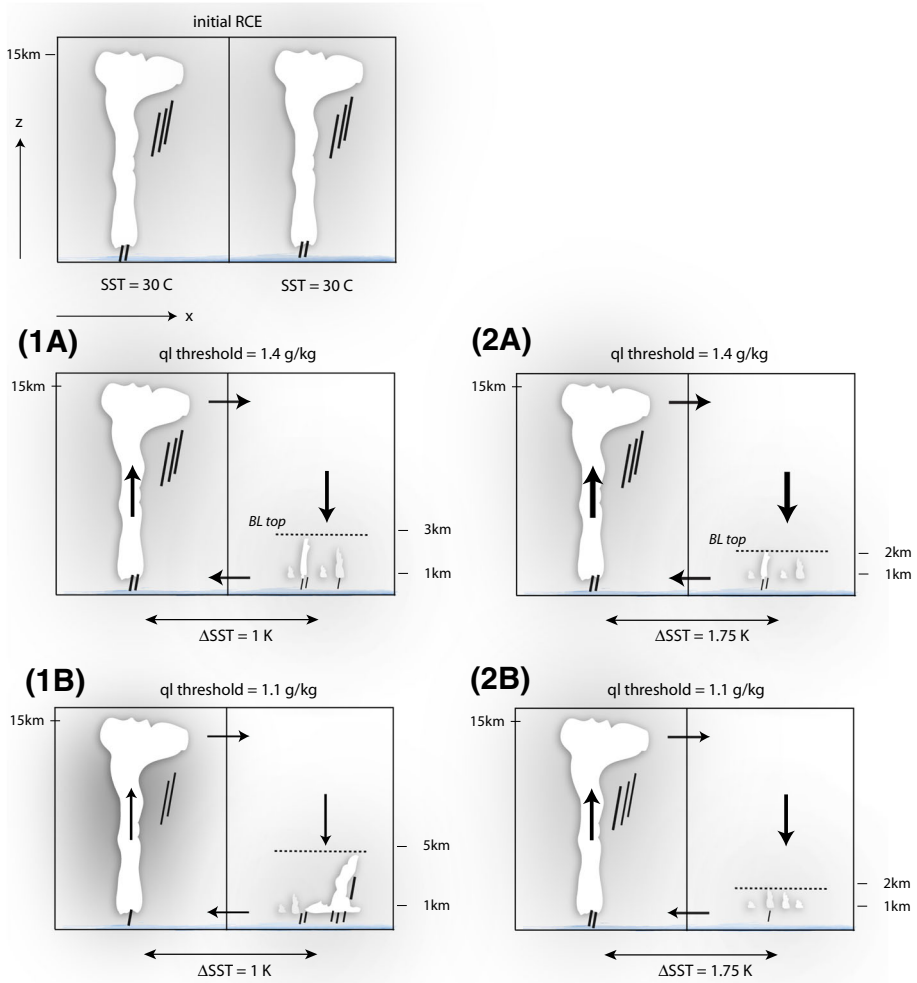


**Fig. 3** A sketch of the two-column overturning circulation with deep convection in both columns in the initial RCE state (top). Below two scenarios are sketched whereby deep convection has developed over the warm ocean and shallow convection over the cold ocean. **1A** and **1B** correspond to a SST difference of 1 K between the columns, and **2A** and **2B** to a SST difference of 1.75 K. In experiment (A) the condensate threshold for rain formation is  $1.4 \text{ g kg}^{-1}$  and in experiment (B) the threshold is  $1.1 \text{ g kg}^{-1}$ . The horizontal dashed lines denote convective tops over the cold ocean. The arrows denote the large-scale vertical velocity in each column and the zonal flow at the column boundary

the zonal wind due to convective momentum transport; and  $\frac{\partial v(\partial \eta / \partial p)}{\partial p}$  represents the momentum flux divergence in the boundary layer, whereby  $v$  is a shear viscosity.

The nonlinear flow is thus forced by zonal gradients in  $\alpha$ , and  $\alpha$  is inversely proportional to the virtual temperature predicted by Eqs. (1) and (2). The Coriolis acceleration is put to zero; hence, the circulation may be considered a mock-Walker circulation. A simple Fickian damping of the flow takes place in the model interior through diffusion at a timescale  $\tau$ . Furthermore, the momentum flux divergence linearly decreases from a maximum damping near the surface to zero damping above the depth of the boundary layer.



**Fig. 4** Sensitivity of convection and precipitation in a Walker-like circulation to the conversion of liquid to rain. The circulation occurs between two columns with different sea surface temperatures (SST), with an increasing SST difference on the  $x$ -axis ( $\Delta$ SST). On the  $y$ -axis are shown: (a) convective tops, (b) surface precipitation rate, (c) column water vapor, (d) equivalent potential temperature ( $\theta_e$ ) of the well-mixed layer, (e) surface wind speed at the column boundary, (f) surface latent heat flux, (g) integral of radiative cooling rate from the surface up to 500 hPa, (h) integral of the virtual temperature gradient ( $\Delta T_v/L$ ) between the columns from the surface up to the convective top in the cold column ( $L$  is the width of one column). Both black lines are for the column over the colder ocean, with dashed lines for a condensate-to-rain threshold of  $1.4 \text{ g kg}^{-1}$ , and solid lines for a threshold of  $1.1 \text{ g kg}^{-1}$  (more efficient warm rain formation). The gray lines are for the column over the warm ocean instead

Momentum is also damped through convective momentum transport. At the surface, a linearized surface drag formula is used as the boundary condition for the horizontal flow, and a free-slip condition is applied at the model top.

The two columns are of equal size and 1500 km wide. A vertical grid of 100 pressure levels is used, with a resolution of about 125 m that becomes finer above 100 hPa. The model integration is performed using a time step of 1 min and continued until equilibrium is reached, usually after 100 days.

Parameterizations are used for the absorption and emission of radiation (Morcrette 1991), for convection and precipitation (Emanuel and Zivkovic-Rothman 1999) and for cloudiness (Bony and Emanuel 2001), which is an extension to the clear-sky-only calculations in Nilsson and Emanuel (1999). The Emanuel convection scheme is based on buoyancy sorting principles, which allows a spectrum of mixtures to ascend or descend to their level of neutral buoyancy. Notably, the scheme does not distinguish between shallow and deep convection and has the ability (in the past deemed a disability) to produce light rain in the absence of deep convection. A simple buoyancy closure determines the mass flux at cloud base, e.g., the mass flux is adjusted to maintain sub-cloud layer air neutrally buoyant when displaced beyond the top of the sub-cloud layer. Surface fluxes are calculated using standard bulk formulae.

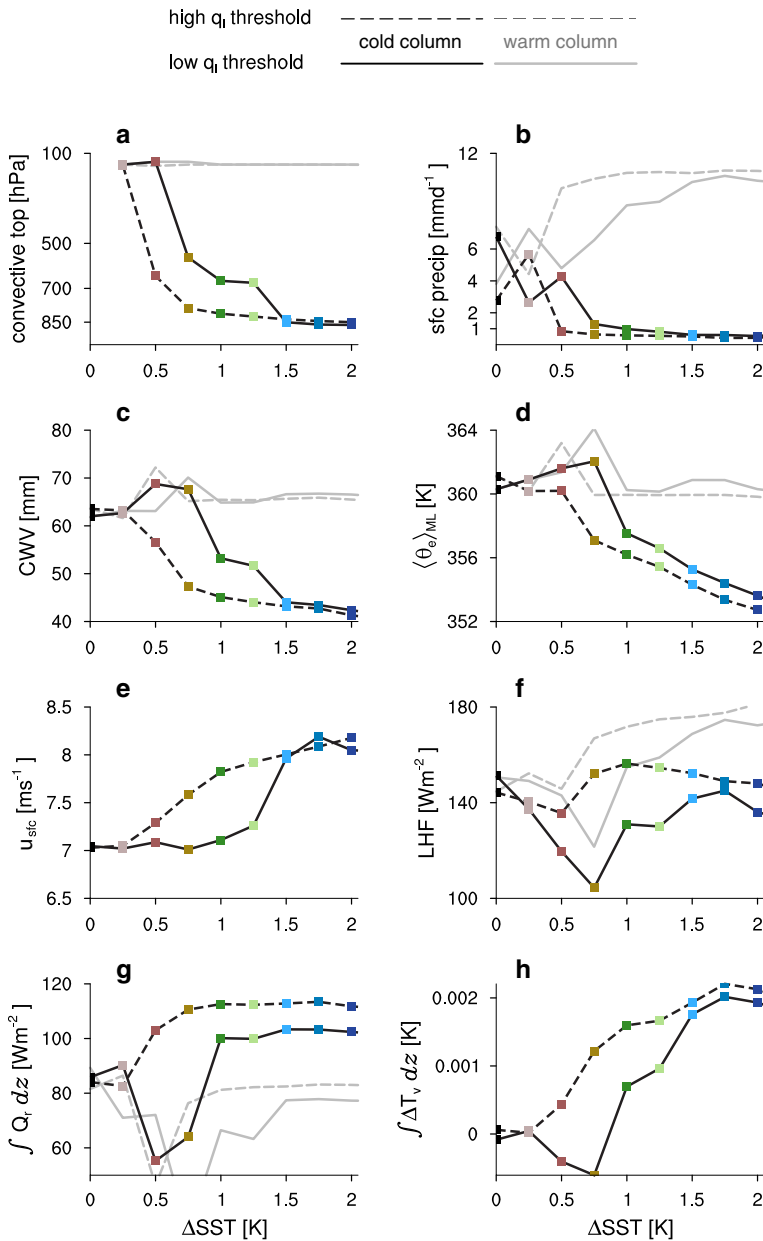
We carry out experiments in which we alter the efficiency of rain formation. The convection scheme has a straightforward way of dealing with (warm) rain formation: all condensate in excess of a temperature-dependent threshold is turned to rain. This assumption is based on the idea that the efficiency of coalescence increases with the amount of condensate and thus the presence of large drops. The threshold is constant up to the freezing level and decreases beyond this level in light of the Bergeron–Findeisen process. Rain and its associated heat are added to a single hydrostatic unsaturated downdraft, and rain evaporates as a function of the temperature and humidity of the environment and the downdraft (Emanuel 1991).

Given the models' physics and lack of a separate boundary layer scheme, our experiments exclude stratocumulus clouds, but we acknowledge that also these shallow clouds produce a significant amount of warm rain that may be relevant to circulating equilibria in the tropical atmosphere (Sect. 1).

## 2.2 Circulating Equilibria in the Two-Column System

A sketch of the two-column system is shown in Fig. 3. The columns are first run into RCE at a uniform prescribed sea surface temperature (SST) of  $30^\circ\text{C}$  (top panel). No circulation exists when both columns have an identical RCE state (top panel). Consequently, the SST in one of the columns is lowered with increments of 0.25 K up to an SST difference ( $\Delta$ SST) of 2 K. Alternatively, we can increase the SST in one of the columns from a colder





RCE state. This gives qualitatively the same results, but some hysteresis is present, because of differences in the initial moisture structure.

The black dashed lines in Fig. 4a show how the tops of convection over the cold ocean collapse with  $\Delta SST$  for a condensate-to-rain threshold of  $1.4 \text{ g kg}^{-1}$ , with blue-hued markers for the largest  $\Delta SST$ . Here, convective tops are defined as the maximum level of positive convective mass flux. For all  $\Delta SST$  convection over the warm ocean remains deep with tops up to 150 hPa (the gray dashed lines). Evidently, a  $\Delta SST = 0.5 \text{ K}$  is enough to

collapse convective tops to roughly 600 hPa (about 4 km), and a  $\Delta\text{SST} = 0.75$  K collapses convection to roughly 800 hPa (about 2 km). Even the shallowest modes produce precipitation with surface rates just below  $1 \text{ mm day}^{-1}$ .

Because convection collapses, the atmosphere above the tops of convection experiences a net (radiative) cooling. This results in a temperature difference with the other column, which triggers a circulation: subsidence develops over the cold ocean ( $\omega_{\text{cold}} > 0$ ) and rising motion over the warm ocean ( $\omega_{\text{warm}} < 0$ ). Near the tropopause the flow is directed from the warm to the cold column ( $u > 0$ ) and near the surface from the cold to the warm column ( $u < 0$ ), as illustrated in Fig. 3-1A, 2A (middle panels) for a SST difference ( $\Delta\text{SST}$ ) of 1, respectively, 1.75 K. A new circulating equilibrium develops in which radiative cooling above the cloud layer over the cold ocean is now balanced by subsidence warming instead of convective heating. Over the warm ocean the mean rising motion introduces extra cooling next to radiative cooling, both of which are balanced by deep convective heating.

Nonlinear behavior at low  $\Delta\text{SST}$ , such as in the surface precipitation rates, are caused by a reverse in the circulation. For  $\Delta\text{SST} \leq 0.5$  K convection over the cold ocean has not yet collapsed, and a weak oscillatory circulation can develop. Furthermore, the convection scheme favors detrainment near mid-levels, which can produce large cloud fractions that significantly lower radiative cooling in the lower troposphere, and also reverse the circulation.

The profiles of  $\omega$  and  $u$  over the cold ocean show how divergence and near-surface wind speeds increase with  $\Delta\text{SST}$  (Fig. 5), but saturate as  $\Delta\text{SST} > 1.5$  K, and even weaken again at very large  $\Delta\text{SST} = 5$  K. The strength of the circulation may be understood through a simplified form of the equation for the flow’s vorticity (Eq. 3). For non-rotating flow and ignoring horizontal advection, damping, surface friction and convective momentum transport, we may write:

$$\frac{\partial \eta}{\partial t} = \frac{\partial \alpha}{\partial x} + \frac{\partial}{\partial p} \left( v \frac{\partial \eta}{\partial p} \right) \tag{6}$$

The first term on the right-hand side measures the buoyancy gradient between the columns and tends to increase the vorticity. The second term is the momentum flux divergence in the boundary layer. This shear stress tends to decrease the vorticity, but may be assumed to vanish at the top of the convective layer. Hence, if we integrate from the surface  $p_s$  up to

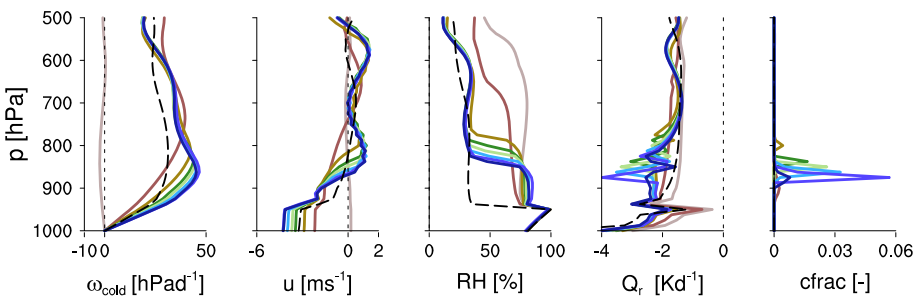


**Fig. 5** Vertical profiles of the vertical velocity  $\omega$ , the horizontal wind speed  $u$ , the relative humidity RH, the heating tendency due to radiation  $Q_r$  and the cloud fraction, for circulations at  $\Delta\text{SST}$  between 0.25 and 2 K. Colors correspond to those used in Fig. 4. All profiles are for the column over the colder ocean surface and for the higher threshold of condensate-to-rain conversion ( $1.4 \text{ g kg}^{-1}$ )

the top of the boundary layer  $p_h$  and rearrange the stress term to the left-hand side, we can write:

$$v_s \left( \frac{\partial \eta}{\partial p} \right)_s = \int_{p_s}^{p_h} \frac{\partial \alpha}{\partial x} dp \quad (7)$$

The term  $\left( \frac{\partial \eta}{\partial p} \right)_s$  on the left-hand side represents a measure of the strength of the circulation.

Equation (7) thus shows how the circulation is not only a function of  $\Delta SST$ , but of buoyancy differences over the entire boundary layer  $h$ . Those buoyancy differences are strongly regulated by the radiative cooling ( $Q_r$ ) over the cold ocean, which changes as the free troposphere dries with increasing  $\Delta SST$ , which is best seen from the RH profiles in Fig. 5.  $Q_r$  tends to peak where temperature and moisture gradients and cloudiness are large, for instance at the inversion and at the mixed layer top (950 hPa). The maximum in  $Q_r$  increases as the inversion lowers. Larger cloudiness below the inversion can do so, but alone the interaction of long wave radiation with the clear-sky humidity profile would be sufficient (for example, see Stevens et al. 2017 in this same book collection). Large increases in  $\Delta SST$  further dry the convective layer, leading to less liquid water and cloudiness, and therefore less radiative cooling and a weaker circulation (black dashed lines, Fig. 5).

In these experiments condensate is turned into rain at a threshold of  $1.4 \text{ g kg}^{-1}$ . For liquid water lapse rates at these temperatures, a threshold of  $1.4 \text{ g kg}^{-1}$  is exceeded after about 600 m. A lower threshold of  $1.1 \text{ g kg}^{-1}$  is exceeded after about 450 m, which is a small difference, but one which has a relatively large impact on the character of convection and the circulation at intermediate  $\Delta SST$ s (the black solid lines in Fig. 4). Convection still collapses, but is more stepwise, with convective tops preferably located near 600 hPa at  $\Delta SST$ s = 1 K, indicative of congestus clouds. Although convective tops are higher and column water vapor increases (Fig. 4c), surface precipitation rates remain near or below  $1 \text{ mm day}^{-1}$  (Fig. 4b).

Also in nature surface precipitation rates slowly increase with column water vapor values between 20 and 60 mm and only pick up beyond a critical value (Holloway and Neelin 2009). One idea that could explain the slow increase in surface precipitation is that in order for precipitation and latent heating to increase, the atmosphere would need to cool more or warm less. Less warming could result from weaker subsidence as congestus develops. However, subsidence warming is still largely balanced by  $Q_r$ , and  $Q_r$  itself decreases as congestus deepens the moist layer.

In the next two sections, some more details of the changes in circulation for the shallow cumulus mode at  $\Delta SST = 1.75 \text{ K}$  (Fig. 3-2A, B) and the congestus mode at  $\Delta SST = 1 \text{ K}$  (Fig. 3-1A, B) are discussed.

## 2.3 Shallow Cumulus

At large  $\Delta SST$  ( $\geq 1.5 \text{ K}$ ) the cold ocean column develops shallow cumulus with tops up to 850 hPa and surface precipitation rates  $< 1 \text{ mm day}^{-1}$ , suggestive of light rain or drizzle. For this shallow mode, experiments with a condensate threshold of 1.4 and  $1.1 \text{ g kg}^{-1}$  are notably similar. However, when looking closely a few interesting differences can be seen, further illustrated with vertical profiles of the difference in potential temperature between low and high condensate thresholds ( $\Delta \theta$ ), and profiles of specific humidity, radiative cooling, convective heating and the vertical velocity (Fig. 6). The

dashed and solid lines refer to experiments with  $q_l$  thresholds of  $1.4 \text{ g kg}^{-1}$ , respectively,  $1.1 \text{ g kg}^{-1}$ .

Convection is slightly shallower when rain formation is more efficient ( $q_l = 1.1 \text{ g kg}^{-1}$ ), and the surface precipitation rate is marginally smaller (Fig. 4b). The vertical humidity profile shows that the boundary layer is also a little shallower with a moister sub-cloud and cloud layer ( $\langle \theta_c \rangle_{ML}$  in Fig. 4d,  $q$  in Fig. 6). Accordingly, the surface evaporation is lower (Fig. 4f). The evaporation of cloud condensate takes place in a somewhat thinner and stronger inversion layer, with a stronger peak in cooling. As we will discuss later, in Sect. 3, these results are consistent with LES studies, which show that rain regulates inversion height by removing condensate that would otherwise deepen the boundary layer.

Because of shallower convection, the integrated buoyancy difference between the two columns is smaller (Fig. 4h). Without any change in the viscosity, this implies a weaker circulation (Eq. 7). The maximum  $\omega_{\text{cold}}$  at  $h$  is smaller, along with smaller  $\omega_{\text{cold}}$  throughout the rest of the troposphere. Less subsidence drying leads to a slightly moister free troposphere, consistent with somewhat lower radiative cooling rates.

For the congestus mode the change in the circulation with warm rain efficiency can be explained in a similar manner, as we will see next. However, in that regime convective tops

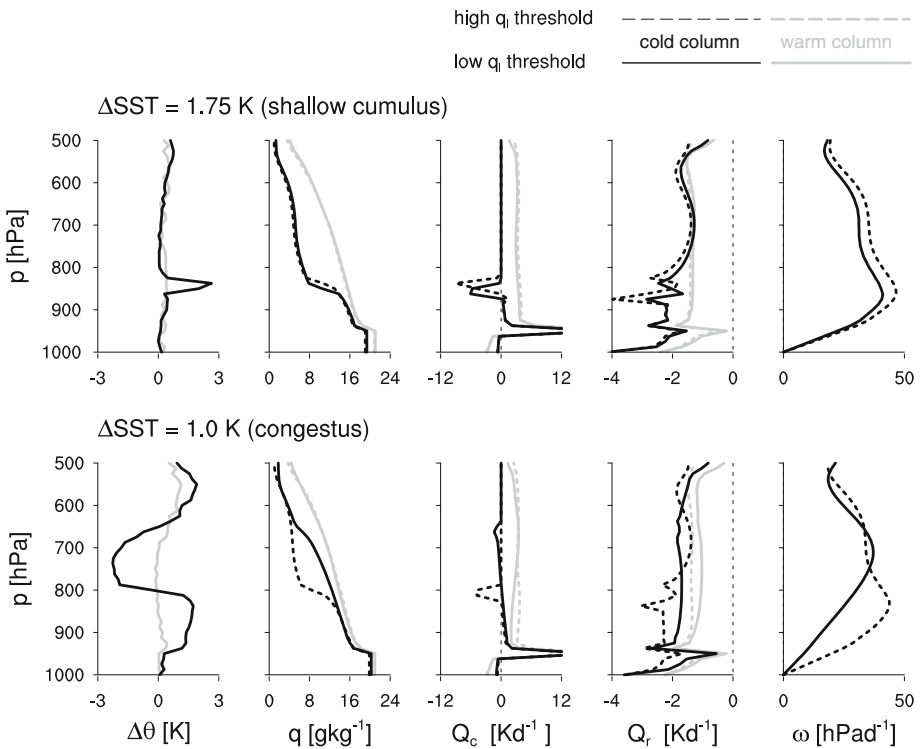


**Fig. 6** For the circulations in Fig. 4 at  $\Delta\text{SST} = 1$  and  $1.75 \text{ K}$  we show vertical profiles of the difference in potential temperature between the two experiments  $\Delta\theta = \theta_{q_l=1.1} - \theta_{q_l=1.4}$ , specific humidity  $q$ , the heating tendency due to convection  $Q_c$ , the heating tendency due to radiation  $Q_r$  and the vertical velocity  $\omega$ . Black and gray lines are for the cold, respectively, and warm column, and solid and dashed lines are for the low, respectively, and high threshold on liquid water for conversion to rain

increase with more efficient rain formation and are accompanied by larger changes in circulation and convection over the warm ocean.

## 2.4 Congestus

For  $\Delta\text{SST}$  between 0.75 and 1.5 K convection is more sensitive to the change in condensate-to-rain threshold. More efficient rain formation ( $q_l = 1.1 \text{ g kg}^{-1}$ ) gives rise to deeper convection and larger surface precipitation rates (Fig. 4). When more condensate is turned to rain, at a lower altitude, updraft buoyancy increases. For  $\Delta\text{SST} = 1 \text{ K}$  a marginal increase in convective heating  $Q_c$  can be seen between cloud base (950 hPa) and 850 hPa with more efficient rain formation (Fig. 6). The level where convective heating turns into cooling has shifted upward, and most of the detrainment and evaporative cooling takes place at cloud tops near 650 hPa. At this level, where cooling is pronounced, subsidence peaks.

Again, the change in condensate-to-rain threshold is small, yet important in this scheme where convection is modeled based on buoyancy sorting principles. Each mixture of air ascends or descends to its level of neutral buoyancy, which might involve several episodes of mixing, especially when precipitation changes the amount of condensate during ascent/descent. Dealing with multiple mixing episodes is bypassed in the current scheme by insisting that mixed air detrains at levels where its liquid water potential temperature is equal to that of the environment (Emanuel 1991). This is illustrated in Fig. 7, which shows the liquid water potential temperature (or liquid water static energy  $h_w$ ) of a lifted parcel ( $h_{w,p}$ , dashed lines) and that of the environment ( $h_w = h$ , solid lines) before mixing.  $h_{w,p}$  is conserved and equal to the dry static energy  $h$  of the sub-cloud layer when there is no precipitation and no mixing. But upon precipitation  $h_w$  increases. In this case, the lower condensate-to-rain threshold of  $1.1 \text{ g kg}^{-1}$  has almost shifted the liquid water static energy of lifted parcels at  $\Delta\text{SST} = 1 \text{ K}$  to that of lifted parcels at  $\Delta\text{SST} = 0.5 \text{ K}$ . Indeed, these two experiments have almost similar congestus tops (Fig. 4a). In other words, the SST is crucial at setting convective tops, but the precipitation efficiency may allow convection over colder SSTs to reach a similar depth as convection over warmer SSTs.

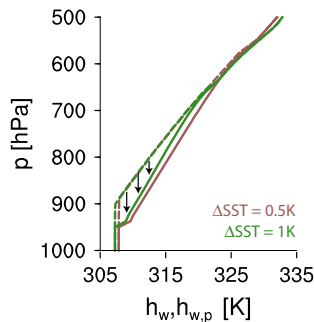


**Fig. 7** The liquid water static energy of the environment  $h_w$  (solid lines), and of a lifted parcel  $h_{w,p}$  before mixing (dashed lines), as calculated in the convection scheme. Two sets of lines are shown, which both represent the column over the colder ocean: one for the experiment with  $\Delta\text{SST} = 1 \text{ K}$  and a threshold of  $1.1 \text{ g kg}^{-1}$  (green) and one for the experiment with  $\Delta\text{SST} = 0.5 \text{ K}$  and a threshold of  $1.4 \text{ g kg}^{-1}$  (brown). The arrows indicate the levels at which the parcel would detrain upon mixing in this scheme. Increasing  $h_{w,p}$  implies that air will not descend as far before detraining

Along with these changes, the thermodynamic structure over the cold ocean, the circulation, and the character of convection over the warm ocean change. For instance, at a threshold of  $1.1 \text{ g kg}^{-1}$  the mixed layer has a larger equivalent potential temperature ( $\theta_e$ , in Fig. 4d). The larger mixed layer  $\theta_e$  can be explained by less low-level radiative cooling, a decrease in subsidence drying and more precipitation. For the congestus modes, the larger mixed layer  $\theta_e$  is accompanied by larger column water vapor (Fig. 4c), which is also evident from the deeper moist layer in the vertical profiles in Fig. 6. Similar to the shallow cumulus mode, the circulation decreases in strength at a lower condensate-to-rain threshold. Whereas for the shallow mode the reduction in  $h$  helps explain the weaker circulation (Eq. 7), in the congestus regime the reduced humidity gradient (followed by the temperature gradient) is responsible for a smaller buoyancy gradient and a weaker circulation (Fig. 4h).

One may question if the response to warm rain efficiency is the same if there were no interaction between the two columns, i.e., when the circulation is fixed and there is no feedback of subsidence to latent heating. LES studies of shallow convection generally impose a fixed subsidence rate and therefore constrain the depth of convection a priori. If we fix the profile of  $\omega_{\text{cold}}$  (using the profile of the experiment with a threshold of  $1.4 \text{ g kg}^{-1}$ ) and run a single-column experiment with a lower threshold of  $1.1 \text{ g kg}^{-1}$  convection is shallower instead of deeper (green lines in Fig. 8). To balance the fixed moderate subsidence warming while having larger latent heating in the cloud layer, the model has to find a new equilibrium with larger radiative cooling in the cloud layer. This layer will be shallower, with a stronger inversion and a drier overlying free troposphere. In this case, the response is similar to that of the shallow mode and similar to LES studies discussed in Sect. 3.1.

The circulation is thus critical to the impact of warm rain in the subsiding column. It leads to small changes in deep convection over the warm ocean. As convection over the cold ocean precipitates more, convection over the warm ocean precipitates less (Fig. 4b). Less precipitation is consistent with a weaker circulation and less cooling from mean vertical ascent over the warm ocean. There is also less cloud-base mass flux, more detrainment and larger cloud fractions near 400 hPa (Fig. 8j, k), which leads to less radiative cooling at low and mid-levels (Fig. 8n).

An intricate interaction between convection, rain microphysics, radiation and the circulation is thus responsible for congestus modes in the two-column model. In the next section, we turn our focus to reviewing some ongoing efforts in fine-scale modeling of convection and space-borne observations, which may be used to address ideas suggested by the two-column model. What limits the congestus modes at mid-levels specifically is discussed in more detail in an upcoming manuscript (Nuijens and Emanuel, in preparation), along with a longer discussion on the influence of model resolution, domain size and the momentum of the flow.

### 3 From a Conceptual Model to Nature

The two-column model suggests that changes in the depth of convection and warm rain in subsiding regions may be accompanied by changes in convection in ascending regions. The model also suggests that small-scale processes such as mixing and warm rain formation, followed by feedbacks through the circulation, have a noticeable impact on the character of convection and the circulation. But in our setup we have made a number of simplifications,

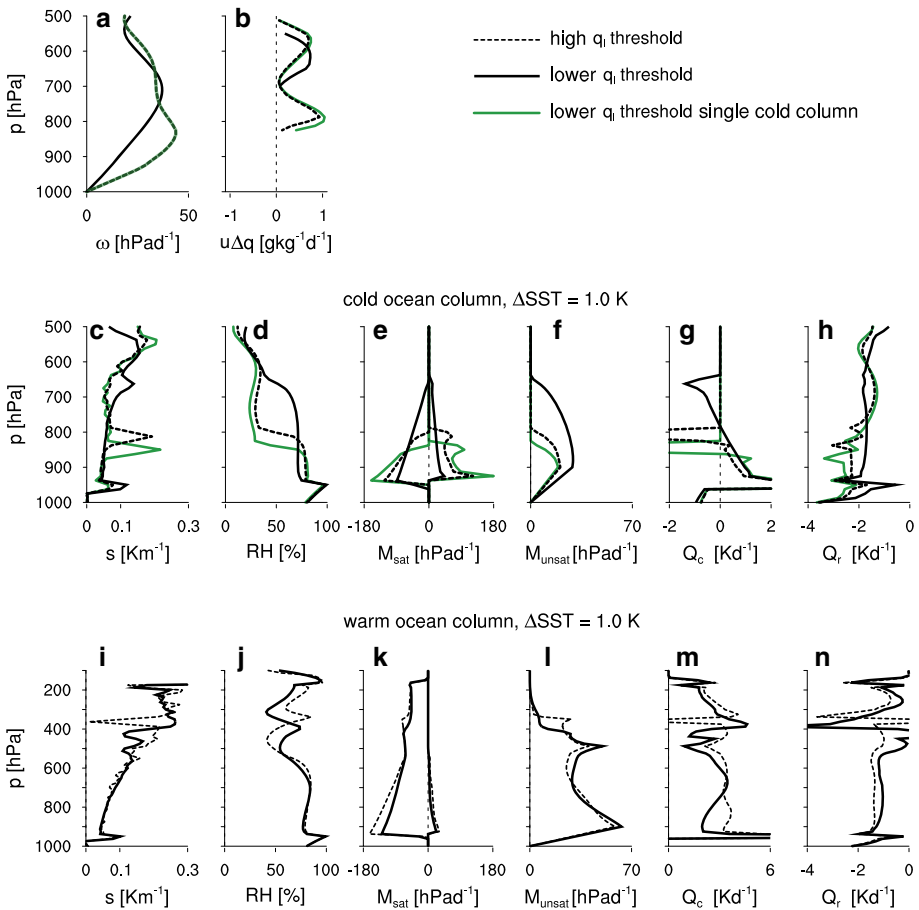


**Fig. 8** Vertical profiles of circulation, convection and thermodynamic structure for the experiment with  $\Delta SST = 1$  K, which develops congestus with more efficient rain formation. Solid and dashed black lines correspond to condensate-to-rain thresholds of 1.1 and 1.4 g kg<sup>-1</sup> (same as in the bottom panel of Fig. 6). Green lines show an experiment with a threshold of 1.1 g kg<sup>-1</sup> but fixed  $\omega_{cold}$  and near-surface  $u$  and fixed moisture convergence. The latter are taken from the experiment with a 1.4 g kg<sup>-1</sup> threshold. Shown are: (top panel) the vertical velocity and moisture convergence, and (middle and bottom panels) the potential temperature lapse rate  $s$ , relative humidity, the saturated mass flux  $M_{sat}$ , both upward and downward components, the unsaturated mass flux driven by precipitation falling outside of the cloud  $M_{unsat}$ , convective heating  $Q_c$  and radiative cooling  $Q_r$

most importantly that the columns are of equal size. As suggested by Pierrehumbert (1995) and Bellon and Le Treut (2003), an important follow-up to this study would be to change the relative size of the columns, or even adding columns. Our findings also crucially depend on the parameterized convection and cloudiness. Hence, our findings should be interpreted as ideas, which need further testing with models that explicitly simulate convection.

For instance, cloud-resolving models (CRMs) that are run on very large domains, even spanning ocean basins, may be forced with a surface temperature gradient to study the sensitivity of circulations to convection (Bretherton et al. 2006). In another approach,



CRMs on two domains may be used to simulate convection explicitly, and the two domains can be coupled through a circulation derived from the weak-temperature gradient approximation (Daleu et al. 2012).

Because shallow convection and cloudiness occur on scales smaller than conventional CRM grids, Large-Eddy simulations (LESs) may be preferred to investigate warm rain implications. So far LESs have been run on domains too small for circulations to develop, and too small for convection to organize itself into moist clusters surrounded by dry regions—a process that may crucially impact climate (Pierrehumbert 1995; Mauritsen et al. 2012). Nevertheless, LES studies have given some insight into the influence of warm rain on the thermodynamic structure of the lower atmosphere. We shall discuss these in the next section and draw out similarities with the two-column model results. Furthermore, we discuss how ground-based or airborne observations may help constrain warm rain formation, which remains uncertain even in LES.

### 3.1 Large-Eddy Simulations

Large-Eddy simulation has long been a tool to study turbulent flows including the cloudy boundary layer on limited horizontal domains ( $20 \times 20 \times 4 \text{ km}^3$ ) at fine grids ( $100 \times 100 \times 40 \text{ m}^3$ ). LES is also increasingly used to simulate deeper convection (up to 10–12 km) on horizontal domains of  $50 \times 50 \text{ km}^2$  and larger and with global-scale simulations underway. Microphysics in LES are typically parameterized using either a bulk scheme, which prognoses one or two moments of the drop-size distribution (only the total mass of rain, or the mass and number of rain drops), or a bin scheme, which uses a discretized version of the drop-size distribution and attempts to model the full evolution of the droplet spectrum. For the bulk schemes, the total cloud mass is inferred from an equilibrium assumption and the cloud droplet number is specified. Hence, these schemes implicitly assume an aerosol or cloud condensation nuclei concentration. By varying the cloud droplet number concentration, the sensitivity to warm rain formation has been studied.

Such sensitivity studies have demonstrated that at larger cloud droplet number concentrations shallow cumuli get deeper before they rain (Stevens and Seifert 2008; Seifert et al. 2015). Therefore, larger cloud droplet number concentrations produce less rainfall initially. But the response of clouds and the boundary layer will mitigate this initial effect. Namely, the removal of liquid water via rain reduces evaporative cooling and mixing near cloud tops and thus the entrainment of warm free tropospheric air into the boundary layer and the deepening of convection and the boundary layer. Therefore, after a long enough (>30 h) simulation time, differences in cloud and rain statistics for different cloud droplet number (aerosol) concentrations are small (Xue and Feingold 2006).

The regulation of inversion height by warm rain has been noted in early bulk theories of shallow cumulus convection and also matters for the sensitivity of shallow cumuli to global warming scenarios. Larger SSTs and less large-scale subsidence under global warming lead to a deepening of shallow cumuli. This increases the entrainment of dry air into the boundary layer, which dries the cumulus layer drier and reduces cloud fraction. But rainfall puts a notable limit to such deepening, so that changes in cloudiness with global warming are overall small (Blossey et al. 2013; Bretherton et al. 2013; Vogel et al. 2016).

In the two-column model, the response of the shallow mode to more efficient warm rain (Fig. 6, top panels), as well as the response of the congestus mode under fixed subsidence (Fig. 8, green lines), is similar to these LES studies. But in LES the subsidence rate is

generally fixed. Our two-column model experiments suggest that changes in subsidence with (latent) heating can change the response to rain at SSTs that are favorable for congestus.

A recent study using LES demonstrates processes that are important in the transition from a shallow to a congestus regime, and we may use these to loosely evaluate changes in atmospheric structure produced by the two-column model. Vogel et al. (2016) and Vogel and Nuijens (in preparation) use a constant exponential profile of subsidence, prescribed SSTs and interactive radiation, for a model domain of  $51.2 \times 51.2 \times 10 \text{ km}^3$  with a resolution of 50 m in the horizontal and 10 m in the vertical. To reproduce many of the differences in cloud and boundary layer structure that are observed during months with predominantly shallow or deeper convection (congestus), an increase in SST and decrease in subsidence (at a reference scale height) are sufficient.

A 2K increase in SST and  $1.5 \text{ mm s}^{-1}$  decrease in  $\omega$  lead to a deepening of convection from 2 to 7 km, a quadrupling of surface precipitation and a 15% decrease in cloud cover. The cloud and boundary layer structure of these control (CTL) and CTL.2K. $\omega$ 6 simulations is shown in Fig. 9 and reveals that as congestus develops, moisture and temperature are much better mixed in the vertical, and the inversion is weaker. Because the inversion is weaker, less cloudiness develops near the inversion.

Critical to reproducing the character of convection and cloudiness in the two regimes is the role of interactive radiation, which can both stabilize and destabilize convection (Vogel and Nuijens, in preparation). For instance, interactive radiation is crucial for stabilizing convection and developing the stratiform outflow layers near the inversion for the CTL simulation. Sometimes interactive radiation also leads to a response one might not expect. For instance, when the free troposphere is drier, convection gets deeper and rains more. This is illustrated with the DRY simulation in Fig. 9, which has  $1 \text{ g kg}^{-1}$  less water vapor in the free troposphere. This enhances the radiative cooling in the moist convective layer and inversion layer, which boosts the buoyancy of cloudy updrafts that reach those layers. As congestus develops and moisture is mixed over a deeper layer, radiative cooling within the cloud and sub-cloud layer and its maximum value decrease (Fig. 9e). Because of the deeper moist layer, the surface latent heat flux also decreases (Fig. 10). Both factors—less destabilization from radiative cooling and a lower surface latent heat flux—could imply that convection self-limits itself. However, in these simulations there is no feedback

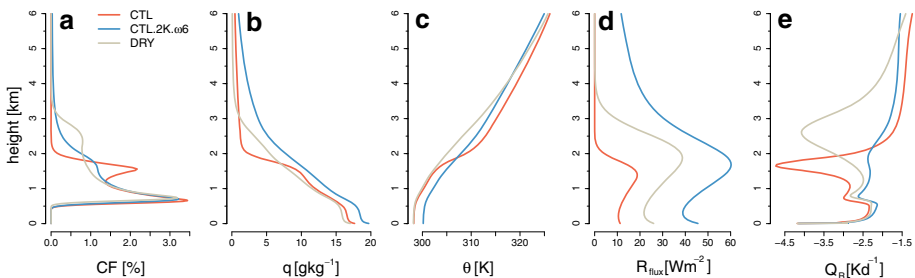


**Fig. 9** Domain-averaged profiles of cloud fraction, specific humidity, potential temperature, precipitation flux and radiative cooling from LES. The CTL (orange) and DRY (gray) simulations differ only in their initial profile of specific humidity in the free troposphere, whereby the CTL run is about  $1 \text{ g kg}^{-1}$  more humid. The CTL.2K. $\omega$ 6 (blue) simulations has a 2K larger SST and a  $1.5 \text{ mm s}^{-1}$  reduction in the prescribed  $\omega$  profile compared to the CTL simulation

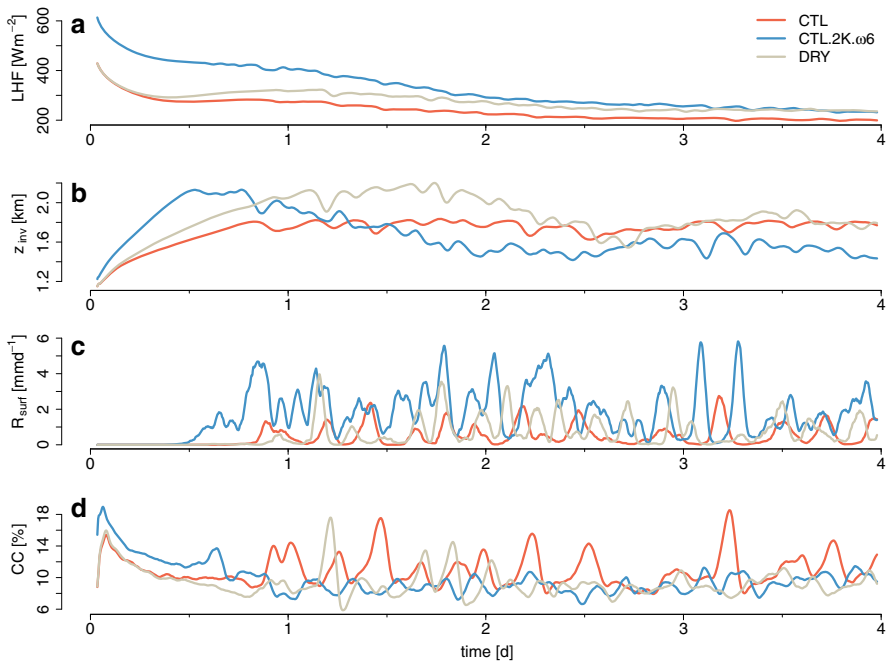


**Fig. 10** Time series of the surface latent heat flux, the inversion height, the surface precipitation rate and total cloud cover for the CTL (orange), DRY (gray) and CTL.2K. $\omega$ 6 (blue) simulations shown in Fig. 9

through the circulation such as in the two-column model, where the reduced cooling leads to a weakening of subsidence.

Average surface rain rates for the congestus clouds in LES are between 20 and 40  $\text{W m}^{-2}$  (Fig. 10). But the simulated rainfall is very intermittent, which is caused by the limited number of deeper clusters and cold pools that this domain size can support. The profile of the rain flux also shows that a fraction of rain evaporates in the lower cloud and sub-cloud layer (Fig. 9d). The evaporation of rain triggers downdrafts which pull down cooler air that can spread out in the sub-cloud layer like a density current (cold pools). Such cold pools have been long known to exist for deep convection (see also Zuidema et al. in this collection). Within cold pools convection is suppressed, but at the downwind (colliding) boundaries of cold pools new convection can be triggered. This leads to arch-shaped cloud formations with clear skies in between as seen from satellite imagery (Snodgrass et al. 2009; Zuidema et al. 2012), and which the LES reproduces. The cold pools from shallow cumuli and congestus are mostly dry in their center, similar to deep convection, because rain rates are sufficiently strong to bring down relatively dry air from higher altitudes. This is different from the cold pools observed in open cell stratocumulus decks, which tend to be moist instead. At what rain rates either dry or moist cold pools develops and for which fraction of rain falling through unsaturated air are still open questions. And even in LES rain microphysics still carry a considerable uncertainty (VanZanten et al. 2011; Seifert and Heus 2013; Li et al. 2015). LES development would thus greatly benefit from progress made in deriving vertical profiles of rain and cloud from ground-based remote sensing networks, which we discuss next.

### 3.2 Observations

*Relationships Between Cloud and Rain* Estimates of how much condensate is turned into rain would help validate microphysical models used in LES, which in turn could help inform models of rain for large-scale models, such as the simple condensate-to-rain threshold used in the convection scheme in the two-column model. Useful first steps would be estimating how much water is removed via rain. Surface measurements of rainfall over a larger area (such as from a weather radar), alongside measurements of surface evaporation (from buoys or ships), and measurements of advection (from sounding arrays) could provide such estimates. For instance, during the Rain in Cumulus over the Ocean (RICO) field campaign surface precipitation rates comprised about a fifth of the surface evaporation rate (Nuijens et al. 2009). The upcoming EUREC<sup>4</sup>A field study (see Bony et al. 2017 in this collection) will provide the measurements needed for such a study.

But surface precipitation rates alone do not reveal at what levels rain has evaporated, or how much rain has fallen through clouds or clear sky. Those differences are important for understanding how moisture is distributed vertically or how convective downdrafts form. This requires better estimates of the vertical profile of the rain flux alongside that of cloud condensate. But an inherent problem is that the profile of cloud condensate and rain cannot be measured simultaneously with a single radar wavelength. Existing methods use a vertically pointing cloud radar (typically 36 GHz or  $K_a$  band) to measure the sixth moment of the drop-size distribution, which may be turned into a profile of cloud liquid water by using the liquid water path obtained from a microwave radiometer, and by making assumptions on the drop-size distribution. Through synergy of instruments at dedicated field sites (such as the CloudNet network in Europe or the US Department of Energy's Atmospheric Radiation Measurement (ARM) sites), refined algorithms have been developed to do so. Such data sets seem ripe for further exploration, but are not without challenges. As drizzle or rain-sized drops develop the drop-size distribution changes, and assumptions underlying these algorithms need to be adjusted. Furthermore, when rain rates are sufficiently high the (cloud) radar beam will become attenuated, and the microwave radiometer has to be shut down. Hence, to estimate the profile of rain that develops in statistically similar clouds, a radar with a smaller frequency (larger wavelength), which suffers less from attenuation, has to be employed at a nearby location, where it has a similar radar footprint. To accurately estimate rain evaporation, the radar should be almost as sensitive as the cloud radar, and hence, a K or  $K_u$  band radar would be ideal. Unfortunately, this would exclude deep convection whose rain rates can be so high that even a K or  $K_u$  band radar signal will be attenuated.

Globally, the CloudSat Cloud Profiling Radar (CPR) can be used to relate measured cloud top heights to surface precipitation rates. But also this is not straightforward. A 94 GHz W band radar suffers from significant attenuation as rain intensity increases, and surface backscatter remains an issue. A recently Bayesian Monte Carlo algorithm uses a cloud-resolving model database to link observed vertical and integrated measurements of liquid clouds to latent heating structures and precipitation rates at the surface (Nelson et al. 2016). A histogram of surface rain rates of each CloudSat CPR profile, stratified by cloud top heights (Fig. 11), shows that clouds with tops beyond 1.6 km produce rain that reaches the surface (similar to what we infer from Fig. 2). Clouds with tops beyond 2 km clearly produce even higher rain rates, but beyond 3 km, the increase in rain rates is overall small, with the exception of very high rain rates, yet these are very rare.

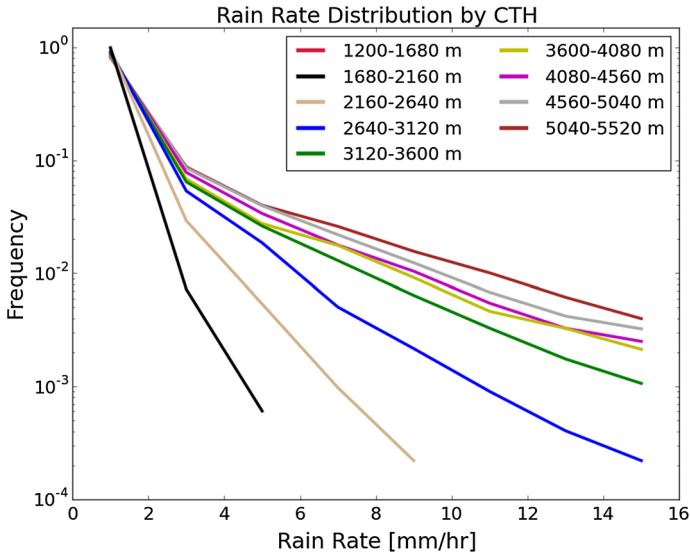


**Fig. 11** Histogram of near-surface rain rates stratified by cloud top heights over tropical oceans as generated with the algorithm of Nelson et al. (2016) using CloudSat CPR data

The successor of the TRMM mission, the Global Precipitation Measurement (GPM) mission, has launched a dual-frequency precipitation radar (DPR) in 2014. This radar has a  $K_a$  and a  $K_u$  band, which suffer less from attenuation than CloudSat's W band. The DPR flies in a non-Sun synchronous orbit with an inclination angle of  $65^\circ$ , allowing it to measure extratropical clouds and the Arctic and Antarctic circles, which TRMM did not sample. Along with a microwave imager, the DPR will measure the vertical structure of precipitation intensities. By combining these measurements with traditional radiometers that already onboard satellites, the GPM mission promises to provide three-hourly rain estimates almost globally (Hou et al. 2013). This will allow studies on relationships between rain and the large-scale flow that can be done on much shorter timescales than has been possible so far.

*Temporal Relationships* One idea suggested by the two-column model experiments is that periods with shallow cumuli and drizzle occur in a different circulation than periods with congestus and rain. Data from the Barbados Cloud Observatory, currently the only remote sensing platform in the tropics, have already demonstrated that congestus and rain vary predominantly on timescales of days to weeks (Nuijens et al. 2014), which suggests that their occurrence is favored during certain large-scale states.

Linking clouds to circulations has been mostly done by long-term averaging of satellite observations over geographical regions or dynamical regimes. But to study variability on daily to synoptic timescales a different approach is needed, because most (polar orbiting) satellites sample a given location too infrequently (one exception being the new GPM mission with its three-hourly precipitation rates globally). One approach is to project different polar orbiting satellites onto a composite time axis centered on a rain event, a strategy that has been used in Masunaga (2013) and Masunaga and L'Ecuyer (2014). The result is a statistical time series on hourly and daily timescales, which precedes and follows those rain events. To illustrate this approach, we can use the areal rain coverage data from TRMM over the subtropical Pacific as a proxy for congestus. This is an area with considerable warm rain (Fig. 1). Because TRMM's minimum detection threshold is 17 dBZ,

much larger than values observed for cloud tops up to 2 km (see also Fig. 2), TRMM likely does not observe drizzle, but only the more intense warm rain showers from congestus. We assume that congestus has an areal rain coverage less than 25%, and use all those events to create the time series in Fig. 12, which shows the evolution of profiles of cloud cover (measured by CloudSat’s CPR), dry static energy and humidity, and the moisture budget.

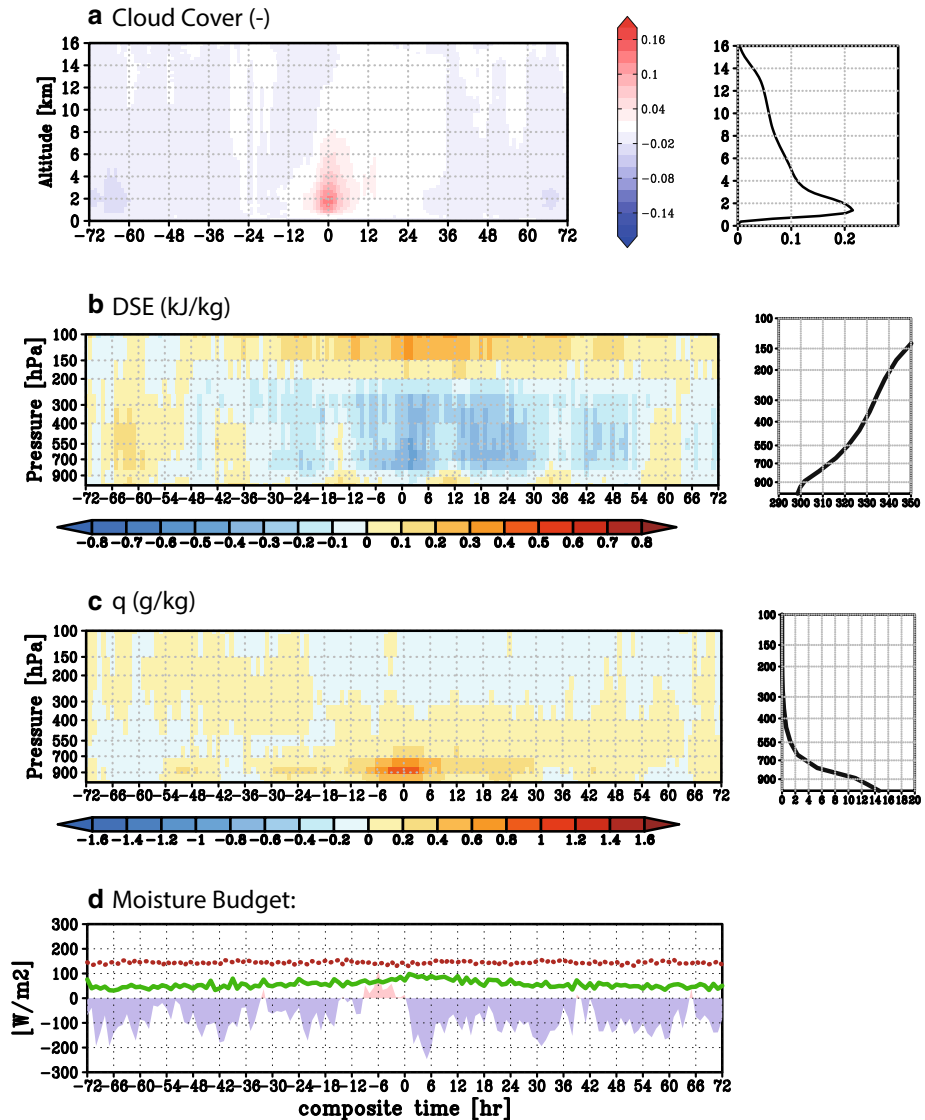


**Fig. 12** Top panel (a) shows a composite time series of CloudSat cloud fraction anomalies from the background state for congestus rain events over the subtropical Pacific at 0 h. Similar composites for the profile of water vapor mixing ratio ( $g\ kg^{-1}$ ) and dry static energy DSE ( $kJ\ kg^{-1}$ ) are shown in panels (b) and (c). The bottom panel (d) shows the composite moisture budget, including the surface evaporation rate (solid green), the surface evaporation (red dotted) and the vertically integrated moisture convergence (in shading, with convergence in light red and divergence in blue)

Figure 12a shows that after the rain event, cloudiness in the lower troposphere is larger for up to 12 h. The surface precipitation rate increases only little at the time of the rain event, which suggests that other precipitating clouds are always nearby (Fig. 12d). We also observe that the surface evaporation is rather invariant, which suggests it does not play a major role in controlling rain, unless its heterogeneity is not captured by the measurements.

Between two days before and after the rain event a cool anomaly in the lower and mid-troposphere is present (Fig. 12b). This cooling can destabilize the atmosphere and promote convection. Furthermore, during and following rain events the lower troposphere moistens, especially up to about 3 km (700 hPa) (Fig. 12c). Radiative cooling might explain the cooling anomalies, because these anomalies (even those in the upper atmosphere 72–36 h preceding the rain event) roughly correspond to the moist anomalies. But without knowing the winds and thus advection, we cannot draw any conclusions yet. This approach should therefore be repeated with additional satellite data, where the zonal wind profiles measured by the upcoming ADM Aeolus mission are particularly interesting. We may also use GPM data, which is more sensitive to light rain, and use cloud top heights instead of rain coverage as proxies for convection.

## 4 Concluding Thoughts

During the last decade, the cloud radar deployed aboard CloudSat has demonstrated that warm rain over oceans is ubiquitous. Recognizing its importance for shallow convection and low-level cloudiness, parameterizations of warm rain formation have been included in high-resolution models, such as LES. LES studies have demonstrated that warm rain can significantly alter the character of shallow convection, such as the depth of clouds, their organization and low-level cloudiness. In turn, shallow convection has been shown to impact large-scale circulations and climate. At least, the radiative driving from low-level cloud has been shown to strengthen large-scale circulations, and differences in low-level cloudiness among GCMs result in different predictions of climate sensitivity. Therefore, in this paper we question how warm rain itself—a process that may alter the character of shallow convection on larger scales—matters for circulations and climate.

We presented new experiments with an idealized two-column model to speculate on the influence of warm rain on tropical circulations. This model solves for two-dimensional non-rotating flow between two columns on a fairly fine vertical grid (125 m) and uses parameterized convection, cloudiness and radiation. Naturally, these parameterizations carry uncertainties, alike those used in GCMs. But the simpler dynamics in the two-column framework allow us to gain some insight into mechanisms involving warm rain, which may serve as a starting point for future studies using models with explicit convection. A circulation with deep convection in one column and subsidence in the other column is forced by prescribing the  $\Delta$ SST between the columns. The circulation and depth of convection in the subsiding column as a function of  $\Delta$ SST are found to depend on an intricate interaction between convection, warm rain, the circulation and radiation. The most interesting findings with respect to the sensitivity to warm rain can be summarized as follows:

1. At large  $\Delta$ SST efficient warm rain formation lowers shallow cumulus tops and the inversion height over the cold ocean. This leads to a small reduction in the integrated buoyancy gradient between subsiding and ascending columns (Fig. 3-2A, B).
2. At smaller  $\Delta$ SST efficient warm rain formation raises shallow cumulus tops, leading to congestus clouds. These congestus clouds are accompanied with deeper moist



boundary layers and a reduction in the integrated buoyancy gradient between the columns (Fig. 3-1A, B).

3. Efficient warm rain formation can thus weaken the circulation across a range of  $\Delta$ SST (but especially at smaller  $\Delta$ SST). Surface precipitation rates over the cold ocean consequently increase, while surface precipitation and cloud-base mass fluxes over the warm ocean decrease.
4. Congestus clouds can develop because of the extra latent heating with more efficient warm rain, which raises parcel buoyancy. But the weakening of the circulation (weaker subsidence) is important for maintaining the congestus mode. Here, the strong reduction of low-level radiative cooling in response to low-level moistening by congestus is crucial.

We may thus postulate that warm rain formation has a negative feedback on the strength of circulations by regulating the depth and thermal structure of the lower troposphere. In other words, raining or deeper shallow cumuli in regions with subsidence may also weaken circulations, besides strengthening them through radiative cooling. An interesting observation in that regard is that periods with stronger near-surface winds are accompanied with deeper cloud layers and significant rain showers (Nuijens et al. 2009, 2015). This could suggest that, as circulations strengthen, convection in the subsiding branches responds by deepening and raining more, which can slow down the circulation.

Because the convection scheme we use is based on the premise that microphysical processes are important for the humidity structure of the atmosphere, a sensitivity to warm rain formation may not be a surprise. Given the uncertainty associated with any convection scheme, the above results should be considered speculative and merely a basis for further testing with models and observations.

An important step forward in improving warm rain processes in models is to use existing ground-based remote sensing. For instance, collocated vertical profiles of cloud and rain from ground-based radar can be exploited to constrain how much cloud condensate detrains and moistens the atmosphere, compared to how much condensate reaches the surface via precipitation. Even in LES such processes remain uncertain. Furthermore, deriving large-scale winds through the use of sounding arrays, combined with intensive vertical profiling of cloud, rain and the thermal structure of the atmosphere, can shed light on relationships between convection and the large-scale flow. These measurements are planned for the EUREC<sup>4</sup>A field campaign (see Bony et al. 2017 in this collection). Finally, to test ideas suggested by the two-column model framework, satellite remote sensing, in particular the new GPM and Aeolus missions, can be used. Namely, these may identify whether long-term variations in circulation strength are linked to variations in rain in subsiding and ascending branches.

**Acknowledgements** This paper arises from the International Space Science Institute (ISSI) workshop on Shallow clouds and water vapor, circulation and climate sensitivity. The first author wishes to express a special thanks to Reimar Luest and the Max Kade Foundation for the opportunity to spend a year at MIT. Thanks go to Ethan Nelson, Raphaela Vogel, Katrin Lonitz and Vivek Sant for their help in creating figures, and to Cathy Hohenegger, Chris Bretherton and Robert Pincus for insightful discussions. Lastly, we thank three reviewers for providing insightful feedback.

**Open Access** This article is distributed under the terms of the Creative Commons Attribution 4.0 International License (<http://creativecommons.org/licenses/by/4.0/>), which permits unrestricted use, distribution, and reproduction in any medium, provided you give appropriate credit to the original author(s) and the source, provide a link to the Creative Commons license, and indicate if changes were made.

## References

- Battan LJ, Brahm RR (1956) A study of convective precipitation based on cloud and radar observations. *J Meteorol* 13(6):587–591
- Bechtold P, Sandu I, Klocke D, Semane N, Ahlgrimm M, Beljaars A, Forbes R, Rodwell M (2014) The role of shallow convection in ECMWFs Integrated Forecasting System. *Ecmwf technicalmemoranda*, ECMWF
- Bellon G, Le Treut HL (2003) Large-scale and evaporation-wind feedbacks in a box model of the tropical climate. *Geophys Res Lett* 30(22):2145. doi:[10.1029/2003GL017895](https://doi.org/10.1029/2003GL017895)
- Berg W, L'Ecuyer T, Haynes JM (2009) The distribution of rainfall over oceans from spaceborne radars. *J Appl Meteorol Climatol* 49(3):535–543
- Blossey PN, Bretherton CS, Zhang M, Cheng A, Endo S, Heus T, Liu Y, Lock AP, de Roode SR, Xu KM (2013) Marine low cloud sensitivity to an idealized climate change: the CGILS LES intercomparison. *J Adv Model Earth Syst* 5(2):234–258
- Bony S, Emanuel KA (2001) A parameterization of the cloudiness associated with cumulus convection; evaluation using TOGA COARE data. *J Atmos Sci* 58:3158–3183
- Bony S, Stevens B, Ament F, Bigorre S, Chazette P, Crewell S, Delanoë J, Emanuel K, Farrell D, Flamant C, Gross S, Hirsch L, Karstensen J, Mayer B, Nuijens L, Ruppert JH Jr., Sandu I, Siebesma P, Speich S, Szczap F, Totems J, Vogel R, Wendisch M, Wirth M (2017) EUREC<sup>4</sup>A: A field campaign to elucidate the couplings between clouds, convection and circulation. *Surv Geophys*. doi:[10.1007/s10712-017-9428-0](https://doi.org/10.1007/s10712-017-9428-0)
- Bretherton CS, Sobel AH (2002) A simple model of a convectively coupled walker circulation using the weak temperature gradient approximation. *J Clim* 15(20):2907–2920
- Bretherton CS, Blossey PN, Peters ME (2006) Interpretation of simple and cloud-resolving simulations of moist convection radiation interaction with a Mock–Walker circulation. *Theor Comput Fluid Dyn* 20(5):421–442
- Bretherton CS, Blossey PN, Jones CR (2013) Mechanisms of marine low cloud sensitivity to idealized climate perturbations: a single-LES exploration extending the CGILS cases. *J Adv Model Earth Syst* 5(2):316–337
- Burdanowitz J, Nuijens L, Stevens B, Klepp C (2015) Evaluating light rain from satellite- and ground-based remote sensing data over the subtropical North Atlantic. *J Appl Meteorol Climatol* 54(3):556–572
- Byers HR, Hall RK (1955) A census of cumulus height versus precipitation in the vicinity of Puerto Rico during the Winter and Spring of 1953–1954. *J Meteorol* 12(2):176–178
- Chen B, Liu C (2015) Warm organized rain systems over the tropical Eastern Pacific. *J Clim* 29(9):3403–3422
- Clement A, Seager R (1999) Climate and the tropical oceans. *J Clim* 12(12):3383–3401. doi:[10.1175/1520-0442\(1999\)012<3383:CATTO>2.0.CO;2](https://doi.org/10.1175/1520-0442(1999)012<3383:CATTO>2.0.CO;2)
- Daleu CL, Woolnough SJ, Plant RS (2012) Cloud-resolving model simulations with one- and two-way couplings via the weak temperature gradient approximation. *J Atmos Sci* 69(12):3683–3699. doi:[10.1175/JAS-D-12-058.1](https://doi.org/10.1175/JAS-D-12-058.1)
- Emanuel KA (1991) A scheme for representing cumulus convection in large-scale models. *J Atmos Sci* 48(21):2313–2329
- Emanuel KA, Zivkovic-Rothman M (1999) Development and evaluation of a convection scheme for use in climate models. *J Atmos Sci* 56:1766–1782
- Haynes JM, L'Ecuyer TS, Stephens GL, Miller SD, Mitrescu C, Wood NB, Tanelli S (2009) Rainfall retrieval over the ocean with spaceborne W-band radar. *J Geophys Res Atmos* 114(D8):n/a–n/a
- Hohenegger C, Stevens B (2016) Coupled radiative convective equilibrium simulations with explicit and parameterized convection. *J Adv Model Earth Syst* 8(3):1468–1482
- Holloway CE, Neelin JD (2009) Moisture vertical structure, column water vapor, and tropical deep convection. *J Atmos Sci* 66(6):1665–1683
- Hou AY, Kakar RK, Neeck S, Azarbarzin AA, Kummerow CD, Kojima M, Oki R, Nakamura K, Iguchi T (2013) The global precipitation measurement mission. *Bull Am Meteorol Soc* 95(5):701–722
- Kato S, Xu KM, Wong T, Loeb NG, Rose FG, Trenberth KE, Thorsen TJ (2016) Investigation of the residual in column-integrated atmospheric energy balance using cloud objects. *J Clim* 29(20):7435–7452
- Kubar TL, Hartmann DL, Wood R (2009) Understanding the importance of microphysics and macrophysics for warm rain in marine low clouds. Part I: satellite observations. *J Atmos Sci* 66(10):2953–2972
- Larson K, Hartmann DL, Klein SA (1999) The role of clouds, water vapor, circulation, and boundary layer structure in the sensitivity of the tropical climate. *J Clim* 12(8 PART 1):2359–2374. doi:[10.1175/1520-0442\(1999\)012<2359:TROCWV>2.0.CO;2](https://doi.org/10.1175/1520-0442(1999)012<2359:TROCWV>2.0.CO;2)

- Lebsock MD, L'Ecuyer TS (2011) The retrieval of warm rain from CloudSat. *J Geophys Res Atmos*. doi:[10.1029/2010JD015415](https://doi.org/10.1029/2010JD015415)
- Li Z, Zuidema P, Zhu P, Morrison H (2015) The sensitivity of simulated shallow cumulus convection and cold pools to microphysics. *J Atmos Sci* 72(9):3340–3355
- Lonitz K, Stevens B, Nuijens L, Sant V, Hirsch L, Seifert A (2015) The signature of aerosols and meteorology in long-term cloud radar observations of trade wind cumuli. *J Atmos Sci* 72(12):4643–4659
- Masunaga H (2013) A satellite study of tropical moist convection and environmental variability: a moisture and thermal budget analysis. *J Atmos Sci* 70(8):2443–2466
- Masunaga H, L'Ecuyer TS (2014) A mechanism of tropical convection inferred from observed variability in the moist static energy budget. *J Atmos Sci* 71(10):3747–3766
- Mauritsen T, Stevens B, Roeckner E, Crueger T, Esch M, Giorgetta M, Haak H, Jungclaus J, Klocke D, Matei D, Mikolajewicz U, Notz D, Pincus R, Schmidt H, Tomassini L (2012) Tuning the climate of a global model. *J Adv Model Earth Syst*. doi:[10.1029/2012MS000154](https://doi.org/10.1029/2012MS000154)
- Miller RL (1997) Tropical thermostats and low cloud cover. *J Clim* 10(3):409–440. doi:[10.1175/1520-0442\(1997\)010<0409:TTALCC>2.0.CO;2](https://doi.org/10.1175/1520-0442(1997)010<0409:TTALCC>2.0.CO;2)
- Morcrette JJ (1991) Radiation and cloud radiative properties in the European Centre for medium range weather forecasts forecasting system. *J Geophys Res Atmos* 96(D5):9121–9132
- Muller CJ, Held IM (2012) Detailed investigation of the self-aggregation of convection in cloud-resolving simulations. *J Atmos Sci* 69(8):2551–2565
- Neggiers RAJ, Neelin JD, Stevens B (2007) Impact mechanisms of shallow cumulus convection on tropical climate dynamics. *J Clim* 20(11):2623–2642
- Nelson EL, L'Ecuyer TS, Saleeby SM, Berg W, Herbener SR, van den Heever SC (2016) Toward an algorithm for estimating latent heat release in warm rain systems. *J Atmos Ocean Technol* 33(6):1309–1329
- Nilsson J, Emanuel K (1999) Equilibrium atmospheres of a two-column radiative–convective model. *Q J R Meteorol Soc* 125:2239–2264
- Nuijens L, Stevens B, Siebesma ap (2009) The environment of precipitating shallow cumulus convection. *J Atmos Sci* 66(7):1962–1979
- Nuijens L, Serikov I, Hirsch L, Lonitz K, Stevens B (2014) The distribution and variability of low-level cloud in the North-Atlantic trades. *QJRM* 140:2364–2374
- Nuijens L, Medeiros B, Sandu I, Ahlgrimm M (2015) Observed and modeled patterns of covariability between low-level cloudiness and the structure of the trade-wind layer. *J Adv Model Earth Syst* 7(4):1741–1764
- Peters ME, Bretherton CS (2005) A simplified model of the Walker circulation with an interactive ocean mixed layer and cloud-radiative feedbacks. *J Clim* 18(20):4216–4234
- Pierrehumbert RT (1995) Thermostats, radiator fins, and the local runaway greenhouse. *J Atmos Sci* 52(10):1784–1806. doi:[10.1175/1520-0469\(1995\)052<1784:TRFATL>2.0.CO;2](https://doi.org/10.1175/1520-0469(1995)052<1784:TRFATL>2.0.CO;2)
- Riehl H, Yeh TC, Malkus JS, la Seur NE (1951) The north-east trade of the Pacific Ocean. *Q J R Meteorol Soc* 77(334):598–626
- Schumacher C, Houze Ra (2003) Stratiform rain in the tropics as seen by the TRMM precipitation radar. *J Clim* 16(11):1739–1756
- Seifert A, Heus T (2013) Large-eddy simulation of organized precipitating trade wind cumulus clouds. *Atmos Chem Phys* 13(11):5631–5645
- Seifert A, Stevens B (2010) Microphysical scaling relations in a kinematic model of isolated shallow cumulus clouds. *J Atmos Sci* 67(5):1575–1590
- Seifert A, Heus T, Pincus R, Stevens B (2015) Large-eddy simulation of the transient and near-equilibrium behavior of precipitating shallow convection. *J Adv Model Earth Syst* 7(4):1918–1937
- Sherwood SC, Bony S, Dufresne JL (2014) Spread in model climate sensitivity traced to atmospheric convective mixing. *Nature* 505(7481):37–42
- Short DA, Nakamura K (2000) TRMM radar observations of shallow precipitation over the Tropical Oceans. *J Clim* 13(23):4107–4124
- Snodgrass ER, Di Girolamo L, Rauber RM (2009) Precipitation characteristics of trade wind clouds during rico derived from radar, satellite, and aircraft measurements. *J Appl Meteorol Climatol* 48(3):464–483
- Stephens GL, Li J, Wild M, Clayson CA, Loeb N, Kato S, L'Ecuyer T, Stackhouse PW, Lebsock M, Andrews T (2012) An update on Earth's energy balance in light of the latest global observations. *Nature Geosci* 5(10):691–696
- Stevens B, Seifert A (2008) Understanding macrophysical outcomes of microphysical choices in simulations of shallow cumulus convection. *J Meteorol Soc Jpn Ser II* 86A:143–162
- Stevens B, Vali G, Comstock K, Wood R, Zanten MCV, Austin PH, Bretherton CS, Lenschow DH (2005) Pockets of open cells and drizzle in marine stratocumulus. *Bull Am Meteorol Soc* 86(1):51–57

- Stevens B, Brogniez H, Kiemle C, Lacour J-L, Crevoisier C, Kiliani J (2017) Structure and dynamical influence of water vapor in the lower tropical troposphere. *Surv Geophys*. doi:[10.1007/s10712-017-9420-8](https://doi.org/10.1007/s10712-017-9420-8)
- Sun DZ, Liu Z (1996) Dynamic ocean–atmosphere coupling: a thermostat for the tropics. *Science* 272(5265):1148–1150
- Takayabu YN, Shige S, Tao WK, Hirota N (2010) Shallow and deep latent heating modes over Tropical Oceans observed with TRMM PR spectral latent heating data. *J Clim* 23(8):2030–2046
- Tompkins AM (2001) Organization of tropical convection in low vertical wind shears: the role of cold pools. *J Atmos Sci* 58(13):1650–1672
- VanZanten MC, Stevens B, Nuijens L, Siebesma AP, Ackerman AS, Burnet F, Cheng A, Couvreux F, Jiang H, Khairoutdinov M, Kogan Y, Lewellen DC, Mechem D, Nakamura K, Noda A, Shipway BJ, Slawinska J, Wang S, Wyszogrodzki A (2011) Controls on precipitation and cloudiness in simulations of trade-wind cumulus as observed during RICO. *J Adv Model Earth Syst* 3(2):M06,001
- Vogel R, Nuijens L, Stevens B (2016) The role of precipitation and spatial organization in the response of trade-wind clouds to warming. *J Adv Model Earth Syst* 8(2):843–862
- Wing AA, Emanuel KA (2014) Physical mechanisms controlling self-aggregation of convection in idealized numerical modeling simulations. *J Adv Model Earth Syst* 6(1):59–74
- Wood R, Comstock KK, Bretherton CS, Cornish C, Tomlinson J, Collins DR, Fairall C (2008) Open cellular structure in marine stratocumulus sheets. *J Geophys Res Atmos*. doi:[10.1029/2007JD009371](https://doi.org/10.1029/2007JD009371)
- Xue H, Feingold G (2006) Large-eddy simulations of trade wind cumuli: investigation of aerosol indirect effects. *J Atmos Sci* 63(6):1605–1622
- Zuidema P, Li Z, Hill RJ, Bariteau L, Rilling B, Fairall C, Brewer WA, Albrecht B, Hare J (2012) On trade wind cumulus cold pools. *J Atmos Sci* 69(1):258–280